NANO LETTERS

Letter

Cite This: Nano Lett. 2018, 18, 2393−2401

pubs.acs.org/NanoLett

# Anisotropic-Strain-Induced Band Gap Engineering in Nanowire-Based Quantum Dots

Luca Francaviglia,[‡] Andrea Giunto,[‡] Wonjong Kim, Pablo Romero-Gomez, Jelena Vukajlovic-Plestina, Martin Friedl, Heidi Potts, Lucas Güniat, Gözde Tütüncüoglu, and Anna Fontcuberta i Morral*

Laboratoire des Matériaux Semiconducteurs, Institut des Matériaux, Ecole Polytechnique Fédérale de Lausanne, 1015 Lausanne, Switzerland

Supporting Information

**ABSTRACT:** Tuning light emission in bulk and quantum structures by strain constitutes a complementary method to engineer functional properties of semiconductors. Here, we demonstrate the tuning of light emission of GaAs nanowires and their quantum dots up to 115 meV by applying strain through an oxide envelope. We prove that the strain is highly anisotropic and clearly results in a component along the NW longitudinal axis, showing good agreement with the equations of uniaxial stress. We further demonstrate that the strain strongly depends on the oxide thickness, the oxide intrinsic strain, and the oxide microstructure. We also show that ensemble measurements are fully consistent with characterizations at the single-NW level, further elucidating the general character of the findings. This work provides the basic elements for strain-induced band gap engineering and opens new avenues in applications where a band-edge shift is necessary.

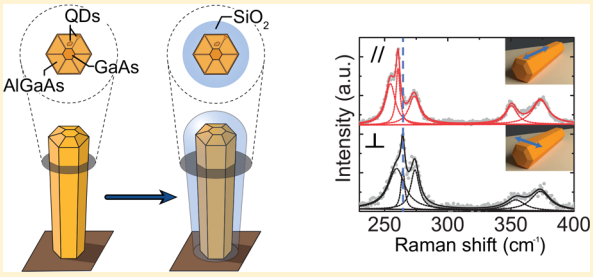


**KEYWORDS:** *Nanowires, quantum dots, strain, oxide, GaAs, PECVD, Raman, photoluminescence*



Semiconductor nanowires (NWs) are very versatile building blocks for optoelectronic devices. As an example, NWs can host material or phase combinations otherwise difficult to obtain in the bulk or in thin films.[3,4] In this way, a plethora of heterostructures including quantum dots (QDs) can be obtained within NWs. The optical performance of the embedded QDs benefits from the tailored shape and size of a NW, e.g., by an enhanced photon extraction[5−8] or detection[9,10] and the potential for an efficient electrical excitation.[11] Several research groups have tried to tune the emission energy of QDs for different purposes. Tuning energy levels involves tuning the absorption/emission, which may be used for sensing, for the storage of information, as well as to facilitate the coupling to cavity modes.[12−15] Strain has shown to be a valuable approach to largely and reversibly tune the emission of QDs.[16] The particular structure and mechanical properties of NWs provide an extended elastic regime, in which strain can be applied.[17−20] The approaches used to apply strain to NW structures include a flexural tensile setup, the use of nanowires as cantilevers, the application of surface acoustic waves, and the deposition of an oxide envelope.[18−23] So far, the latest approach has produced the largest tuning of the emission energy, but the origin of the shift is not clear yet.

Here, we report on a NW-oxide system with QDs embedded in the shell of core−shell GaAs-AlGaAs NWs.[1,2] We provide the first experimental evidence for the presence of strain independently from the redshift of the semiconductor band gap. To do so, we use nonresonant Raman spectroscopy. We also provide experimental support to the fact that the applied strain mainly results in a uniaxial component along the main axis of the NW, in agreement with previous simulations.[22,23] We univocally correlate the strain and the redshift on large and variable ensembles of NWs and QDs and at the single nanowire level, in order to prove the reliability and reproducibility of the chosen technique. We provide understanding on the role of the microstructure and deposition temperature of the oxide. This last result, together with the reproducibility of the straining method, opens the possibility to engineer the band gap and the surface properties of NWs and QDs in NWs. The combination of the two degrees of freedom and the application of different materials suggests the potential of this technique in photoelectrochemical or optoelectronic applications where a band gap modulation and surface protection by an oxide are needed.

**NW-Oxide Straining System.** We start by explaining how to perform strain engineering in NWs and core−shell QDs by applying an external amorphous shell. Figure 1a depicts the schematics of the experiment and the system studied. We can grow NWs both in a self-ordered way[24,25] and in patterned arrays.[26] In both cases, we grow the NWs on silicon to ensure there is no light emission from the substrate. We begin with a GaAs NW obtained by the Ga-assisted method[26−28] and then follow up with the growth of an AlGaAs shell that intrinsically contains self-assembled QDs.[1,2] The QD emission is then tuned by applying a static straining device (Figure 1a), which is a layer

Received: December 23, 2017
Revised: March 14, 2018
Published: March 26, 2018




DOI: 10.1021/acs.nanolett.7b05402
Nano Lett. 2018, 18, 2393−2401

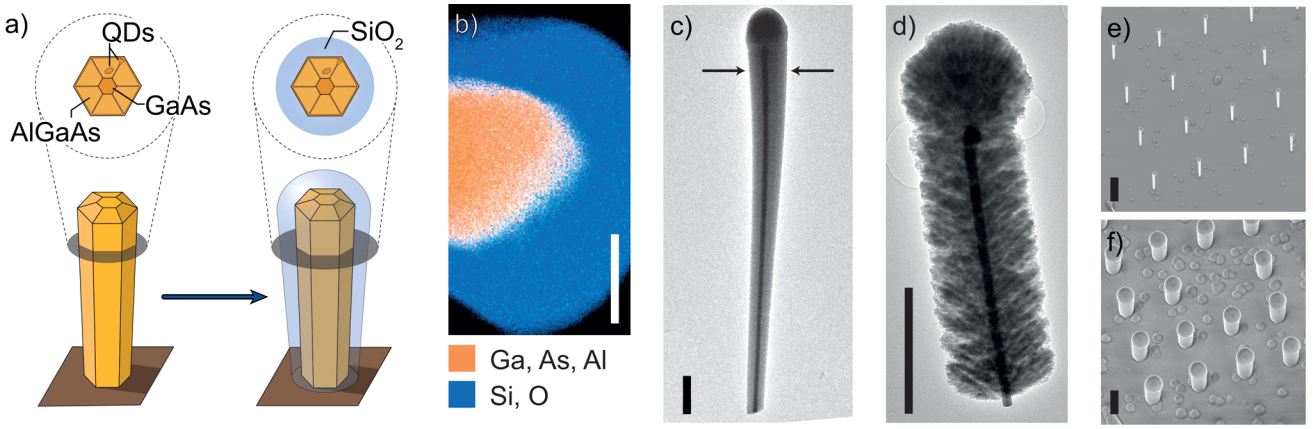


**Figure 1.** (a) Sketch of the NW on growth substrate, uncoated (left) and coated by $SiO_2$ (right). The cross sections above show the QDs in the shell of the NW.[1,2] (b) TEM X-ray energy-dispersive-spectroscopy (EDS) map of the top of a GaAs-AlGaAs NW coated with $SiO_2$. (c) Low-magnification TEM micrograph of a NW coated with $SiO_2$ deposited at 300 °C. (d) Low-magnification TEM micrograph of a NW coated with $SiO_2$ deposited at 100 °C. (e, f) SEM images at 20° tilting of the same NWs in an array, respectively, before and after the coating with 180 nm of $SiO_2$. Scale bars: (b) 100 nm, (c–f) 2 $\mu$m.

of silicon dioxide obtained by plasma enhanced chemical vapor deposition (PECVD). Figure 1b corresponds to the chemical analysis of the III–V/oxide NW-coating structure, indicating a sharp interface between the semiconductor and the oxide.

Figure 1c,d corresponds to typical transmission electron microscopy (TEM) micrographs of NWs, respectively, coated with $SiO_2$ at 300 °C (Figure 1c) and 100 °C (Figure 1d) as a substrate temperature. One observes that PECVD is highly conformal, and the oxide layer follows the geometry of the NW (more details in Supporting Information). However, a microstructure formed by longitudinal grains is visible in Figure 1d and pronounced tapering is also observed in Figure 1c: the oxide thickness gradually decreases from the top to the base of the NW. This gradient is due to both electric-field enhancement at the NW tip and the mutual shadowing of the precursors by neighbor NWs during the deposition. The thicker the nominal oxide thickness is, the more important the tapering becomes. For this reason, we have calibrated the real versus nominal oxide thickness along the NW length (more details in Supporting Information). In the following, we will refer to the $SiO_2$ thickness as the average value measured at the top of the NWs, unless differently specified. The arrows in Figure 1c indicate what we consider as the NW top. We could recognize and address the single NWs before and after the oxide deposition when core–shell GaAs-AlGaAs NWs[1] were grown on site-selected positions on a silicon substrate.[26] Figure 1e,f shows scanning electron microscopy (SEM) micrographs, from exactly the same NWs at the corner of an array, before and after the deposition of 180 nm of oxide. It is interesting to notice that the tapering is absent in the array NWs, as demonstrated by the one in Figure 1d. This is most probably due to the fact that the length of these NWs is shorter (4 $\mu$m) than in the case of the self-assembled NWs (10 $\mu$m), like the one shown in Figure 1c. For a given inter-NW distance, a smaller NW length causes less mutual shadowing and the resulting tapering is reduced or even eliminated.

We characterized the light emission from the QDs by microphotoluminescence ($\mu$-PL) spectroscopy performed on each individual NW, while we studied the oxide-induced strain by means of Raman spectroscopy. Unless differently stated, both PL and Raman spectra were always taken at the same top position indicated in Figure 1c in order to discard any spread in the results related to the variation of the oxide thickness along the NW axis. This choice equally allows us to discard any variations of the QD emission energy along the NW axis.[25]

**Impact of Strain on NWs and QDs.** First, we elucidate the controlled strain by Raman spectroscopy. In particular, we demonstrate that the $SiO_2$ provides a tensile strain along the NW direction. It is well-known that an applied stress field results in a change of the phonon energies of an (Al)GaAs crystal, which can be assessed by Raman spectroscopy.[19,20,29−31] The Raman measurements shown in Figure 2a,c,e were performed at 12 K, on NWs transferred on a Si substrate in the same backscattering configuration as in ref 19. We consider the Lorentzian fit of the peaks in the spectrum of the uncoated NW as a reference. The spectra are composed of two groups of peaks. At high wavenumbers, we find the AlAs-like peaks from the AlGaAs shell (TO 359.5 ± 0.3 $cm^{-1}$ and LO 376.7 ± 0.2 $cm^{-1}$). At lower wavenumbers, we find the GaAs TO mode at 266.4 ± 0.1 $cm^{-1}$[30] and the GaAs-like modes from the AlGaAs-shell (TO 260.3 ± 0.5 $cm^{-1}$ and LO 277.9 ± 0.1 $cm^{-1}$).[32,33] The GaAs LO mode is not present, due to the selection rules.[30,32] The position of the AlAs and GaAs-like LO modes of 5 NWs is consistent with an average Al composition of 29 ± 8%.[34]

All of the Raman modes downshift upon both the oxide depositions shown in Figure 2a. In particular, the GaAs TO mode downshifts by 2.31 ± 0.21 $cm^{-1}$ after the deposition of 180 nm of $SiO_2$ and by 4.41 ± 0.14 $cm^{-1}$ after the deposition of 360 nm of $SiO_2$. This trend follows a linear correlation between downshift and oxide thickness. We thus deduce that the oxide has a clear impact on the strain and that it can be assessed by Raman spectroscopy.

Previous works suggested that the oxide provides anisotropic response along the longitudinal axis of the NW, even under the assumption of isotropic properties of the oxide.[22,23] Here, we provide additional arguments of why the strain should be uniaxial. The TEM micrograph of the NW coated with $SiO_2$ shown in Figure 1d provides some insight. The micrograph clearly shows a granular structure, with oriented grains tilted toward the NW axis. The TEM micrographs of all the NWs show this feature, even when the grains are less pronounced. We believe that this structure results from the impingement direction of atoms and ions during the oxide deposition (Figure



DOI: 10.1021/acs.nanolett.7b05402
Nano Lett. 2018, 18, 2393−2401

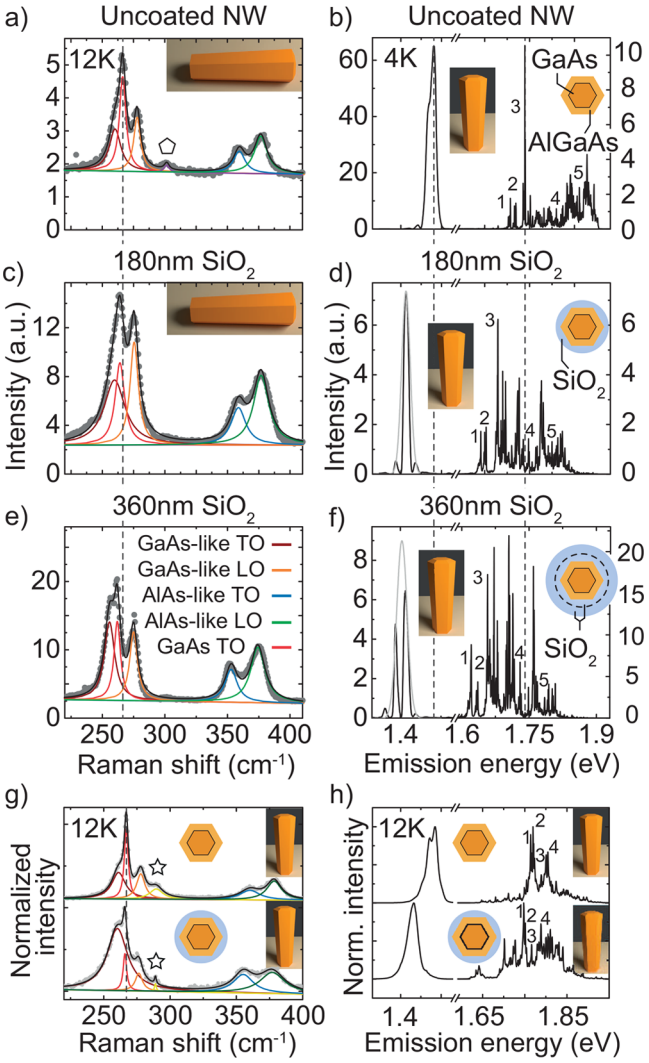


**Figure 2.** From top to bottom: optical measurements on single NWs, respectively, uncoated (a, b), coated with 180 nm of $SiO_2$ (c, d), and with additional 180 nm of $SiO_2$ (e, f), as represented in the sketches in the right corners of panels b, d, and f. (a, c, e) Micro-Raman at 12 K of single NWs. The peaks are fitted by Lorentzian curves. Color-coding legend in panel e. The pentagon in panel a labels the second-order Raman scattering of the Si substrate. The dashed vertical line corresponds to the position of the GaAs TO peak in the uncoated NW as a reference. (b, d, f) $\mu$-PL spectra at 4.2 K of exactly the same array NW. The dashed vertical lines correspond to the emission from the core and the QD line 3 in the uncoated NW. Raman (g) and PL (h) spectra of the very same vertical array NW before and after $SiO_2$ coating. The star in panel g indicates the GaAs LO mode. The color coding is the same as in panel e. The dashed vertical line corresponds to the GaAs TO mode in the uncoated NW (g). Four QD PL lines are labeled in panel h.

1d and more details in Supporting Information). Similar structures have been observed before on NWs coated with permalloy by sputtering.[35] Given this structural anisotropy of the oxide shell, we deduce that the exerted strain is probably anisotropic as well. In particular, a net longitudinal contribution should be considered along the NW growth axis.

We proceed now with the quantification of the strain by evaluating the Raman shifts. For this purpose, we use the model from ref 19. In this work, Signorello et al. applied a controlled uniaxial stress along the longitudinal axis of GaAs NWs, which corresponds to the (111) direction of the zinc-blende (ZB) crystal. This direction is the same as in our case. Eq 1 relates the shift of the GaAs TO mode ($\Delta\omega_{TO}$) with the strain along the NW longitudinal axis ($\epsilon_{zz}$):

$$\epsilon_{zz} = \frac{\Delta\omega_{TO}}{\omega_{TO}} \frac{1}{[-3\gamma_T H + r'_T(1-H)]} \quad (1)$$

with

$$H = \frac{1-2\nu}{3}$$

$\omega_{TO}$ is the relaxed phonon frequency in $cm^{-1}$ for the GaAs TO mode, $\gamma_T = 1.35$ and $r'_T = -0.88$ are respectively the hydrostatic and deviatoric mode Grüneisen parameters[19] and $\nu = 0.16$ is the Poisson ratio for GaAs (111). We use the same Grüneisen parameters as for bulk GaAs because a minor difference was reported,[19,31] while we utilize the Poisson ratio found for GaAs NWs in the (111) direction.[19] We use the same parameters for all temperatures, as no substantial difference has been reported for measurements at lower temperatures.[19] The shift of the GaAs TO mode is consistent with a tensile strain of 0.54 ± 0.06% and 1.04 ± 0.08% upon, respectively, the first and second deposition of 180 and 360 nm of $SiO_2$. Given the brittle behavior of GaAs at low temperatures, it is remarkable that the NWs do not break under such a high strain.[36] It is likely that the high surface-to-volume ratio and the absence of bulk and surface defects increase the fracture stress in the NWs.[17] Further support to the calculation of strain by means of eq 1 will be provided in the following by the measurements on NW ensembles.

We address now the impact of strain on the optical properties of the NWs and QDs. Figure 2b,d,f reports the $\mu$-PL spectra performed exactly on the same NW upon successive coatings with $SiO_2$. The top spectrum (Figure 2b) corresponds to the NW-QD structure before any oxide deposition. The two spectra below (Figure 2d,f) were taken after depositions of 180 nm each time, for comparison with the same oxide thickness as in the Raman spectra in Figure 2a,c,e. The PL spectra were acquired at 4.2 K, with the laser incident on the top of vertical NWs.

In each $\mu$-PL spectrum, we distinguish emission of two different origins. The broader emission around 1.5 eV corresponds to the free exciton emission from the GaAs NW core. It mainly originates from GaAs in the ZB phase. In the top spectrum of the uncoated NW, the peak exhibits a small shoulder at lower energies, which may be due to the presence of few crystal twins and few wurtzite (WZ) segments. The intensity modulation is attributed to Fabry–Pérot resonances,[37] and it is particularly visible in the samples coated with $SiO_2$. The emission clearly redshifts for an increasing oxide thickness. We have fitted the peaks with a Gaussian curve to assess the energy shift upon $SiO_2$ deposition. In particular, we fitted the two peaks in the PL of the uncoated NW with two Gaussian curves, while in the other PL spectra the Gaussian curves fit the maxima of the Fabry–Pérot resonances. The first deposition results in a redshift of about 68 meV, while the second deposition brings an additional redshift of about 9 meV. One should note that the second deposition results in the oxide completely filling the space between the NWs. We think that this changes the straining conditions with respect to the case in which the single NWs are enveloped by independent oxide



DOI: 10.1021/acs.nanolett.7b05402
Nano Lett. 2018, 18, 2393–2401

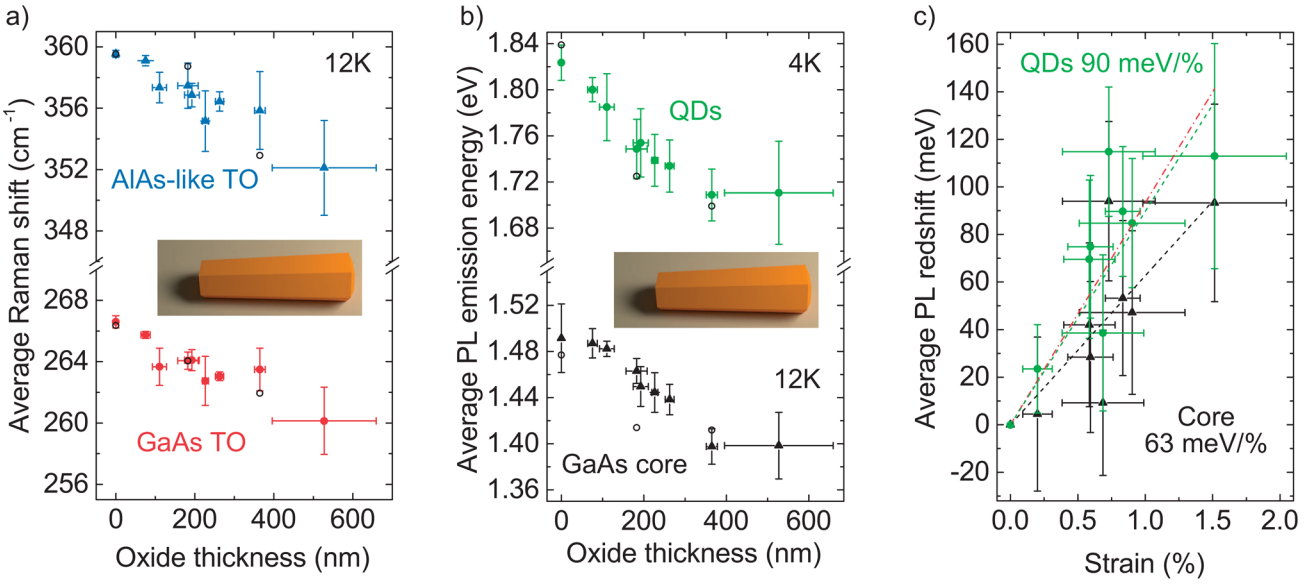


**Figure 3.** (a) Average GaAs TO (red circles) and AlAs-like TO (blue triangles) Raman shift of horizontal NWs at 12 K vs oxide thickness. All error bars are the standard deviations of the distributions. (b) QD emission energy acquired by PL on ensembles of horizontal NWs at 4.2 K vs oxide thickness. The horizontal error bars are the standard deviations of the oxide thickness distributions. Average of the emission energy of the QDs (green circles) and GaAs core (black triangles) distributions with the standard deviation as a vertical error bar. The open black circles in panels a and b are the values of the corresponding quantities derived from the single-NW spectra in Figure 2a,b. (c) Average QD (green circles) and core (black triangles) PL redshift vs strain. The dashed green and black lines are a linear fit of, respectively, the QD and the core PL redshift. The dash-dotted red line corresponds to the theoretical redshift of the heavy-hole band gap recombination in GaAs NWs.[19]

shells. In turn, we think that this can explain the smaller redshift of the core emission after the second deposition.

The group of narrow lines at higher energy in the spectra in Figure 2b,d,e originates from the QD emission in the NW AlGaAs shell. Due to the excitation depth of the laser, we excite several QDs simultaneously.[1,2] One advantage of measuring the same single NW is that we can follow the evolution of individual emission lines. Some illustrative peaks at different energies are labeled as 1, 2, 3, 4, and 5. Also, in this case, a redshift is qualitatively visible. As quantitative examples, the peak fits of the lines 1, 2, 3, 4, and 5 all give a redshift between about 60 and 73 meV upon the first deposition. The second deposition brings and additional redshift between about 7 and 21 meV. There is no apparent correlation between the redshift and the initial QD emission energy. On the contrary, both the core and all measured QD lines redshift more after the first deposition. As already mentioned, the second deposition is less effective probably because the oxide completely fills the space between the NWs.

Interestingly, we notice an overall increase in both the Raman and PL intensity after coating the NWs, which is already visible in the spectra in Figure 2a–f (more details in Supporting Information). We believe that this positive effect depends on the smoother transition in the refractive index between the vacuum and the NW in the presence of $SiO_2$.[38]

Figure 2a–f shows the cumulative effect of the $SiO_2$ deposition on the Raman and PL spectra of the NWs. In order to corroborate the link between the Raman downshift and the PL redshift, Figure 2g,h corresponds to the same vertical NW. We acquired Raman and PL spectra at the same temperature (12 K) before and after the deposition of 110 nm of $SiO_2$. We observe that the GaAs TO peak downshifts by slightly more than 1 cm$^{-1}$ and the GaAs LO by about 0.6 cm$^{-1}$; the PL emission of the QD 3 in Figure 2h redshifts by 23 meV and the core PL by about 37 meV. The PL redshift is in reasonable agreement with the Raman downshift measured on the same NW. As expected for 110 nm of $SiO_2$, these shifts are lower than those obtained for 180 nm of $SiO_2$ and shown in Figure 2c,d. No relevant difference is present between the PL spectra acquired at 4 K (Figure 2b,d,f) and those acquired at 12 K (Figure 2g,h).

**Nature of Strain.** In order to provide more precise evidence of the nature of strain, we turn to the systematic study of larger ensembles of NWs. Measurements on large NW ensembles provide a statistically robust support to the results obtained on single NWs and confirm the reproducibility of the results. For this, the NW structures were grown in a self-organized manner on the Si substrates as in refs 2, 24, and 25. A large-area sample was divided into nine pieces. Each piece underwent the deposition of a $SiO_2$ coating of a different thickness, excluding one kept as an uncoated reference. The oxide thickness ranged between 75 and 527 nm, as characterized by TEM. For these Raman and PL measurements on large ensembles, we dispersed the NWs onto silicon substrates.

We chose 5 NWs for each oxide thickness to perform Raman measurements at 12 K. Figure 3a shows the average peak position of two TO modes as a function of the thickness of the oxide in each subsample. The peak position was derived from Lorentzian fits, like in Figure 2a (more details in Supporting Information). The error bars represent the standard deviations. Here, we show only the evolution of the GaAs TO and AlAs-like TO modes for clarity. The GaAs TO mode is independent from the percentage of Al in the shell. Similarly, the AlAs-like TO mode has an almost flat dependence on the Al content in the AlGaAs alloy.[34] Therefore, we expect that the peak position of these modes depends only on the strain in the NW, and we use the GaAs TO mode as a gauge of the applied strain. Figure 3a shows that the Raman peaks downshift for increasing oxide thickness in a linear way. The Raman downshift confirms the



DOI: 10.1021/acs.nanolett.7b05402
Nano Lett. 2018, 18, 2393–2401

increase in tensile stress applied by an increasing thickness of the oxide, which, in turn, redshifts the PL emission energy. We notice a broadening of the vertical error bar in the graph of Figure 3a. This broadening is a consequence of the larger variability in the oxide properties for thicker depositions, like local changes in thickness and density. Indeed, it actually highlights the large impact of the oxide shell against minor variations in the properties of the oxide and the NW. Considering the average GaAs TO peak, we measure a maximum downshift of 6.45 ± 2.22 $cm^{-1}$ between the uncoated NWs and those coated with the thickest oxide (measured thickness of 527 nm on average).

We performed $\mu$-PL measurements at 4.2 K on 25 NWs from the same ensembles prepared for Raman spectroscopy. Figure 3b shows the average emission energy of the NW GaAs core and shell QDs as a function of the measured oxide thickness. The error bars are the standard deviations of the emission distributions. Both the QD and the core PL redshifts are clearly visible and maximized by the second-to-last deposition with respect to the uncoated NWs (measured oxide thickness of 365 nm). The average QD position shifts by ∼115 meV, while the GaAs core by only ∼94 meV. The shifts are significantly larger than the dispersion given by the error bars. Both the horizontal and vertical error bars in Figure 3b increase for thicker oxides. This observation reflects the increase in the variability of the oxide properties in thicker depositions. Yet, the overall trend of the graph is clear, and it supports the fact that the applied strain is large enough to overcome minor variations in the properties of the oxide and the NWQDs.[39−41] Theoretical predictions and experiments show that the pressure coefficient of AlGaAs at the Γ point increases with the Al content in the composition range of our interest.[34,42] As a consequence, one can deduce that, for a given strain, the AlGaAs band gap redshifts more than the one of pure GaAs. This fact can account at least in part for the difference in the overall redshift of the core and the QDs, which is visible in Figure 3b. Moreover, one should take into account that, in the case of the QDs, strain does not only redshift the AlGaAs band gap in which the QD potential well is set. Strain can also decrease the confinement by changing the QD shape and decreasing the QD potential barrier. This second consideration is supported by the aforementioned increase in the pressure coefficient in the presence of Al.[34,42] The QD barriers redshift more than the Al-poor QD well. Therefore, the confinement on the excitons trapped in the QDs is smaller, which provides an additional redshift.

It is also interesting to focus on the onset of the PL redshift of the QDs and the core. The core PL shows a first slope that seems to get steeper after the first two depositions. According to ref 19, uniaxial stress along [111] lifts the GaAs crystal symmetry and light- and heavy-hole bands split; in particular, the heavy-hole band redshifts more than the light-hole one. Under a small strain, the two bands are still close enough in energy to contribute to the PL emission.[19] Under a larger strain, only the heavy holes contribute. This transition may be visible as the initial change in slope in the core redshift in Figure 3b. On the contrary, because of confinement, we can assume that QDs only emit by recombination of electron and heavy-hole excitons, that is, with a unique slope.

We turn now to the validation of the strain as mostly uniaxial. For each oxide thickness of the NW ensembles, we calculate the corresponding average strain from the shift of the Raman peaks. Eq 1 is valid for the GaAs TO mode. In Figure 3c, we plot the redshift of the median of the QD and core PL in function of the corresponding strain. We use eq 1 to calculate the strain from the Raman GaAs TO shifts in Figure 3a. In ref 23, the nature and value of the strain are uniform along the NW radial direction. In our case, the data do not seem to indicate otherwise. Therefore, we assume that the strain calculated from the downshift of the GaAs TO peaks corresponds to the strain applied to the QDs as well as to the core. We can calculate a linear fit of the redshift in function of the strain (the dash-dotted green and black lines in Figure 3c, respectively, for the QDs and the core). We obtain that the QD PL shifts by 90 meV/%, while the core by 63 meV/%. The QD redshift is consistent with those already reported for a very similar NW-oxide system.[23] It also agrees with theoretical calculations[19] and with the value found in ref 19, by experiments with a straining system that guarantees the uniaxial nature of the applied stress. Our QD redshift is slightly more pronounced than the experimental one for GaAs.[19] This difference may further support our previous considerations on the loss of confinement in strained QDs and on the increase in pressure coefficient in the AlGaAs matrix.[34,42] Calculations only based on hydrostatic stress[31] lead to inconsistently larger slopes. This comparison discards the purely hydrostatic strain in our case and, together with the agreement with the work of Signorello et al., further validates the conclusion that, effectively, also in our system, the stress is mainly applied as a component along the NW longitudinal axis.

On the other hand, the core PL redshifts less than the theoretical expected value (red dash-dotted line in Figure 3c). We mainly ascribe this discrepancy to the large influence (more details in the Supporting Information) that few twins and WZ segments have on the PL emission energy.[43] In particular, they are responsible for uncontrolled shifts of the PL emission energy from the NW core. Together with the PL shift that may be induced by surface charges trapped at the NW-oxide interface during PECVD, we prefer to rely on Raman spectroscopy to estimate the applied strain.

We provide now further support to the highly anisotropic nature of the strain by polarization-dependent Raman measurements. In Figure 4a,b, we, respectively, show the Raman spectra of an uncoated and a coated NW lying horizontally. We excite the NWs with light linearly polarized along the longitudinal NW axis and alternatively collect the scattered light with a linear-polarization filter aligned parallel or perpendicular to this axis, as sketched in each panel in Figure 4a,b. With this method, it is possible to distinguish the different contributions of the two GaAs TO modes because their degeneracy is lifted under anisotropic stress. The two modes are usually named $TO_S$ and $TO_D$,[44,45], respectively, detected for scattered light with parallel and perpendicular polarization with respect to the NW axis.[19] No splitting is observed between the two configurations for the uncoated NW in Figure 4a. In the case of the coated NWs, the spectrum collected in the perpendicular configuration is clearly shifted with respect to the one collected in the parallel configuration (Figure 4b): the GaAs TO mode in the parallel configuration is at 260.6 $cm^{-1}$, while it is at 264.4 $cm^{-1}$ under perpendicular collection. The difference (3.8 $cm^{-1}$) indicates a smaller strain in the perpendicular direction. One can therefore state that the applied stress is highly anisotropic, and it is mainly applied as uniaxial tension in the direction parallel to the NW longitudinal axis. (See the Supporting Information for more measurements.)

The TO splitting is manifested as broadening in non-polarized Raman spectra. The GaAs TO peak is thus the



DOI: 10.1021/acs.nanolett.7b05402
Nano Lett. 2018, 18, 2393−2401

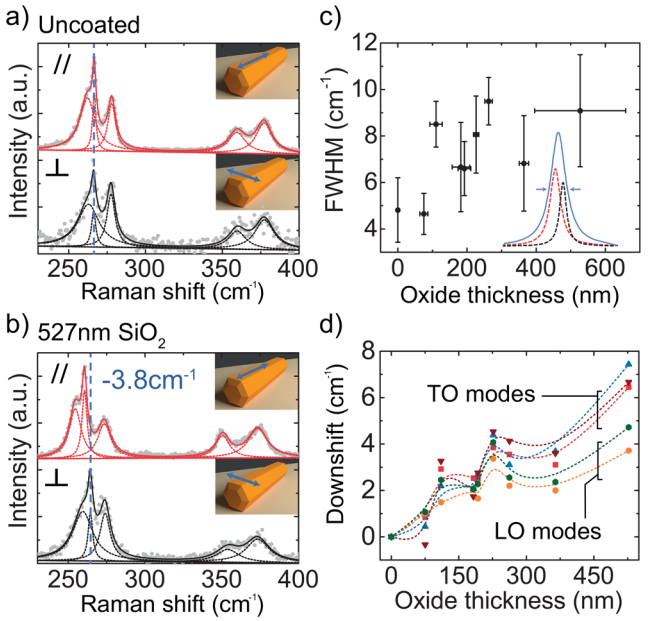


**Figure 4.** (a, b) Polarization-dependent Raman spectra of uncoated (a) and coated (b) horizontal NWs at 12 K. In each panel, the upper curve (red) corresponds to a spectrum taken with both collection and excitation with linear polarization parallel to the NW longitudinal axis, while in the lower curve (black) only the excitation polarization is parallel to the NW longitudinal axis and the collection is perpendicular. The vertical dashed lines correspond to the position of the TO peak in the case of the parallel collection. (c) Average full width at half-maximum (fwhm) of the GaAs TO mode in the Raman spectra taken at 12 K on horizontal NWs vs oxide thickness. The linear polarization of these spectra was not selected. The sketch shows that the mode line width broadens as a consequence of the convolution of the two peaks revealed by polarization-dependent Raman spectroscopy. (d) Average Raman shift with respect to the uncoated NWs for all modes at 12 K vs oxide thickness. The color coding follows the one introduced in Figure 2e. The Raman shift of each mode is referred to those of the uncoated NWs as zero.

convolution of the two contributions. The splitting, and thus the full width at half-maximum (fwhm) of the convoluted spectra, increases with increasing strain. In Figure 4c, we plot the average fwhm of the GaAs TO modes from nonpolarized Raman spectra at 12 K in function of the sample oxide thickness. The line width broadens with the oxide thickness, in agreement with an increase in anisotropy.

In Figure 4d, we plot the Raman shift of all modes from spectra acquired at 12 K on horizontal NWs. We use the position of the modes in the uncoated NWs as zero, in order to compare the downshift of the different modes in the same plot. As expected, one can observe that in the thickest depositions, the downshift of the LO modes is less and less pronounced with respect to one of the TO modes.

In ref 19, the authors estimate the Poisson ratio for GaAs NWs, under the assumption that the deformation potentials are the same as in the bulk. They report a slightly smaller value for NWs ($0.16 \pm 0.04$) with respect to the bulk (0.186), although their result is affected by a large experimental error. We use the results from the polarization-dependent Raman spectra to deduce the Poisson ratio of GaAs and analyze if it changes with the envelope-induced strain or the nanoscale size of the NWs. We obtain an average value of $\nu = 0.19 \pm 0.02$, which highlights no major differences with the bulk (more details on the derivation in the Supporting Information).

**Importance of Oxide Nature.** At the origin of strain, the literature[47] typically distinguishes between intrinsic and extrinsic contributions. Among several cases, the first category includes the structure of the deposited film, while a typical example of the second category is the thermal strain that results from the difference between the thermal expansion coefficient (TEC) of the oxide and the NW.

We now provide considerations on the structure of the oxide and its correlation with strain. In Figure 5, we present the data about four different depositions as illustrative examples out of ten NWs for each case. In particular, Figure 5a–c shows SEM images of array NWs of purely GaAs coated with $SiO_2$ at different substrate temperatures during the PECVD: 100 °C in Figure 5a, 300 °C in Figure 5b, and 400 °C in Figure 5c. By increasing the substrate temperature, the surface morphology of the $SiO_2$ becomes smoother; as expected,[47] the grain structure is less pronounced and the size of the grains decreases. The TEM micrographs in Figure 1c,d of, respectively, a NW coated at 300 and 100 °C confirm this observation. Figure 5e–h report the Raman spectra of the corresponding vertical NWs in Figure 5a–d. For each case, we acquired the Raman spectra at room temperature (RT) before and after the $SiO_2$ PECVD. In this scattering configuration, both GaAs TO and LO are allowed. In addition, a surface optical (SO) mode appears[46,48−50] and splits after the $SiO_2$ deposition. In general, the SO mode shifts because of a change in the dielectric constant at the NW surface.[46,48−50] Once coated, in our NWs, both the strain and the change in dielectric constant control the SO position. However, there is a unique and continuous NW-oxide interface. Therefore, there is also a unique dielectric constant at the NW surface after coating, and the SO split may rather depend on the anisotropic nature of the applied strain. Moving to the analysis of the TO and LO modes, we observe that they all downshift in all three $SiO_2$ depositions. We report the downshifts of the TO modes in blue in the graphs. The downshifts increase from left ($+0.7$ $cm^{-1}$ in Figure 5e) to right ($+4.1$ $cm^{-1}$ in Figure 5g). Therefore, the tensile strain increases together with the deposition temperature. The downshifts are coherent for all ten NWs measured in each sample, except for the deposition at 100 °C. In this case, we observed fluctuations and even upshifts of the Raman modes. We highlight that this effect is not related to the oxide thickness. On purpose, the $SiO_2$ thickness of the depositions at 300 and 400 °C is about 300 nm, and the corresponding Raman shifts are similar. The deposition at 100 °C shows the smallest shift in spite of a larger oxide thickness of about 480 nm.

The evolution of the tensile strain with the $SiO_2$ structure indicates a correlation between the two. In particular, the stiffness of the $SiO_2$ deposited at a lower temperature is reduced. As one can infer from the low-density gaps between two grains in Figure 1d, the large grains obtained at a lower temperature are loosely connected to each other. In this case, the oxide is easily damaged, for instance, during the transfer of the NWs on TEM grids (more details in the Supporting Information). On the contrary, the $SiO_2$ deposited at higher temperatures is more robust. In other words, the $SiO_2$ deposited at 100 °C lacks the necessary solidity to transfer any significant strain to the NWs. Through the grain structure, one can therefore control the stiffness of the oxide and, in turn, the application of the tensile strain. This possibility demonstrates a further degree of freedom in $SiO_2$ PECVD: high-temperature depositions can maximize the applied strain, while a low-temperature deposition may be useful for


DOI: 10.1021/acs.nanolett.7b05402
Nano Lett. 2018, 18, 2393−2401

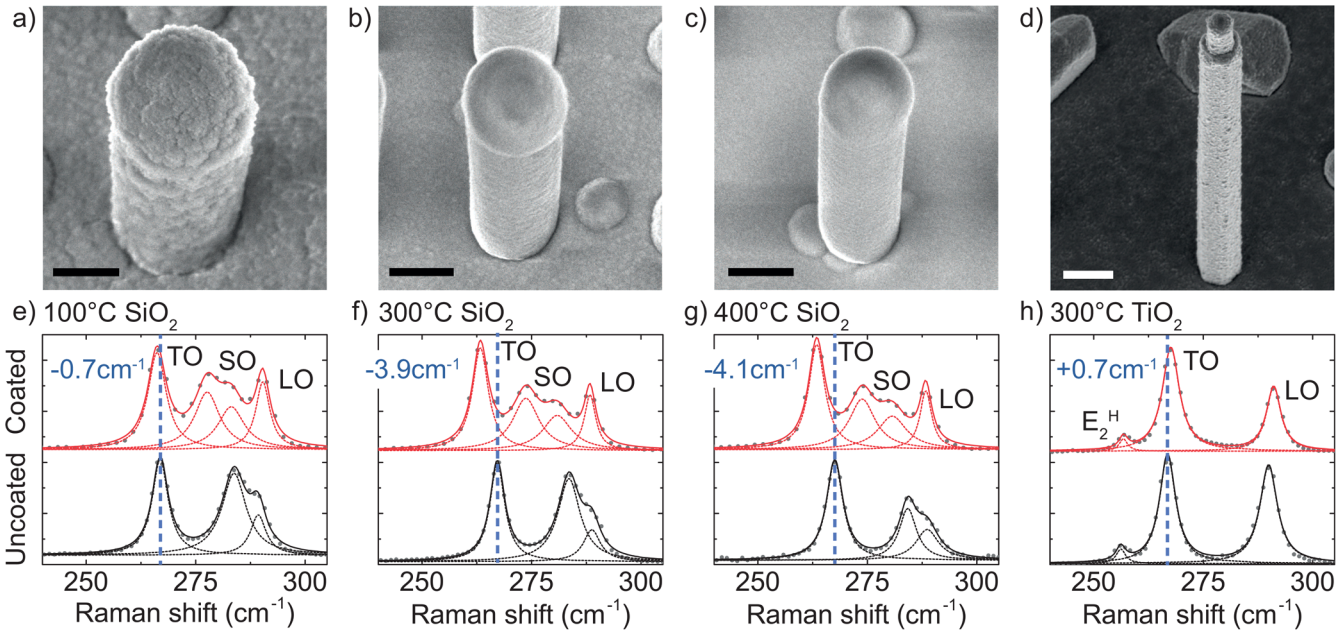


**Figure 5.** (a–d) From left to right: SEM images of GaAs array NWs, respectively, coated with $SiO_2$ at 100, 300, and 400 °C and $TiO_2$ at 300 °C. Scale bars are 500 nm. (e–h) Raman spectra of the NWs from panels a–d in the same order. Black: uncoated NWs. Red: coated NWs. The dashed curves are Lorentzian fits. The TO, LO, $E_2^H$,[30] and surface optical (SO)[46] modes are labeled. The dashed vertical lines in blue correspond to the TO GaAs mode of the uncoated NWs. In blue in the upper left of each plot is the shift of the Raman TO upon coating.

protecting NWs from the environment without changing their optical properties.

At the atomic level, the importance of the oxide structure for the application of strain gets further support in ref 23. Here the authors consider the atom and ion impingement during PECVD and how it forces the atomic bonds of $SiO_2$ in a nonequilibrium configuration. This builds up strain in the oxide itself, which is eventually transferred to the NW. We found in the literature that this can be controlled through the deposition parameters, such as the plasma frequency during PECVD,[51] but we have not further investigated this technical aspect. The authors of ref 23 find that the built-in strain is as important as the strain derived from the thermal dilation. In particular, the TEC of $SiO_2$[52,53] is smaller than the one of GaAs and AlGaAs,[34,54,55] and this agrees with the application of tensile strain to the NW. However, also in our case, the thermal strain cannot account for all of the strain we observe. For instance, there is an almost linear correlation between the thermal strain and the temperature gradient from the deposition temperature to RT, but this is not the trend that we observe from the Raman data in Figure 5. Furthermore, we do not record a larger downshift of the Raman peaks when we further decrease the measurement temperature down to 12 K (more details in the Supporting Information).

Therefore, we conclude that the main working principle of our straining device is the atomic-scale internal strain of the oxide, modulated by the oxide stiffness at the level of its microstructure. Yet, when the internal strain is set to a smaller contribution by adjusting the parameters of the deposition, the thermal strain may play a major role.

We also deposited $TiO_2$ by sputtering in order to further demonstrate the versatility of the same device concept for another deposition technique and another material. We studied an ensemble of 10 NWs before and after sputtering. As an example, in Figure 5d we show the SEM image of an array NW that we sputtered with $TiO_2$ at 300 °C, and in Figure 5h we compare the Raman spectra acquired at RT before and after the deposition. The Raman modes upshift as a consequence of the deposition, which corresponds to a compressive strain. In the Supporting Information, we show the $\mu$-PL response of the NW at RT before and after the $TiO_2$ deposition: the blueshift of the GaAs PL signal further supports the compression of the NW by means of the $TiO_2$ coating. Therefore, we can change the strain from tensile to compressive, and we demonstrate this change with a more general approach than in ref 22.

In conclusion, we presented an efficient and yet simple system to shift the emission of QDs embedded in NWs. The strain can be quantitatively tuned by the thickness of the deposited oxide. We give robust evidence of the reproducibility of the system in spite of the variability of the emission of the NWs and the QDs. By means of Raman spectroscopy, we provide the first experimental proof of the presence of tensile strain independently from the measurements of the redshift of the NW band gap. Raman spectroscopy provides quantitative evidence to evaluate the amount and nature of the applied strain. This would not be possible only with PL measurements because the PL emission energy is sensitive to many more effects, such as surface states and polytypism.[43] We give an experimental estimation of the applied strain in agreement with its uniaxial nature, which we further support by the analysis of the polarization-dependent Raman spectra. We have validated this method for different materials and techniques. Concomitantly, the temperature of the deposition brings a further degree of freedom to the functionalization of the NW-oxide system. This opens the possibility to functionalize the properties of the NWs at the surface while tuning their band gap. This could open new avenues, for instance, in photoelectrochemical applications, in which the band gap of the semiconductor is related to the light absorption but also to the overpotential. Here, the oxide shell would protect the semiconductor from corrosion, and at the same time, it



DOI: 10.1021/acs.nanolett.7b05402
Nano Lett. 2018, 18, 2393–2401

would enable the tuning of the overpotential of the device by strain.

**Experimental Section.** *Nanowire Growth.* We grew the NWs in a DCA P600 MBE machine through the Ga-assisted method[26,27] on Si (111) substrates. More details on the growth of the self-assembled NWs are available in refs 25 and 27, while the detailed growth process of the arrays NWs is available in ref 26.

*Oxide Deposition.* We coated the NWs with $SiO_2$ by PECVD in a PlasmaLab system 100 PECVD by Oxford Instruments. We used a 400 sccm of $N_2$ 98% $SiH_4$ and 710 sccm of $N_2O$ at a radio frequency power of 20 W. We deposited the $TiO_2$ coating in a Pfeiffer SPIDER 600 sputtering machine.

*Morphology and Structure.* We acquired the SEM images in Zeiss MERLIN and Zeiss GEMINI 300 microscopes operated at 3 kV to study the morphology of the NW on their growth substrates. We used FEI Tecnai OSIRIS and FEI Talos microscopes operated at 200 kV on NWs transferred on carbon-coated TEM grids for studying the structure and measuring the thickness of the oxide. By switching to the STEM mode on the FEI Tecnai OSIRIS microscope, we acquired the X-EDS maps.

*Photoluminescence.* For the low-temperature $\mu$-PL spectra, we put the NWs in a close-loop liquid-helium cooled cryostat at 4.2 K. We used a continuous-wave HeNe laser (emission wavelength = 632.8 nm) as an excitation source. We focused the laser light in a 1 $\mu$m large spot on the sample by means of an objective with NA = 0.85. The power density on the samples was in the order of 100 W/cm$^2$. We collected the PL signal through the same objective, dispersed it with a 300l/mm grating and detected it by means of a nitrogen-cooled charge-coupled device (CCD). For the QD PL spectra at RT and the NW-core PL spectra at 12 K, we used a single-frequency optically pumped semiconductor laser at 532 nm wavelength (continuous wave) as an excitation source. We used a microscope objective (NA = 0.75) to focus the laser on the NWs in a spot with a diameter of 1 $\mu$m and a power density of about $10^3$ W/cm$^2$. We collected the PL signal through the same objective and dispersed it with a 300l/mm grating onto a Peltier-cooled CCD.

We analyzed the PL signal from the NW ensembles by means of an automatized code. We acquired the spectra from 25 NWs for each oxide thickness. From each PL spectrum, we calculated, through the code, the median of the emission energy weighted on the intensity of the signal at the different energies. We plotted the average of the medians of the 25 spectra. The standard deviation of the average gave the error bars.

*Raman Spectroscopy.* We collected the low-temperature Raman spectra by putting the NW on the coldfinger of a helium-cooled cryostat at 12 K. We used the same setup as the one for the RT PL, with the difference that we used a power density of about $10^4$ W/cm$^2$ and a triple spectrometer in order to separate the Raman emission from the Rayleigh scattering. A final 1800l/mm grating dispersed the light on a nitrogen-cooled CCD. We realized the measurements in a backscattering configuration with the NWs transferred in the horizontal position on a Si wafer. For the polarization-dependent Raman spectra, we filtered the laser light with a linear polarizer and aligned the selected polarization to the NW main axis by means of a rotator. We used a second polarizer to filter the scattered light.

We collected the RT Raman spectra by means of a commercial Renishaw inVia Raman microscope using the same excitation source as in the low-temperature measurements. We used a grating with 1800l/mm to disperse the light, a notch filter to discard the Rayleigh scattering of the laser, and a Peltier-cooled CCD to detect the signal.

## ■ ASSOCIATED CONTENT

### Supporting Information

The Supporting Information is available free of charge on the ACS Publications website at DOI: 10.1021/acs.nanolett.7b05402.

TEM micrographs of several depositions in different conditions, the calibration of the measured versus nominal oxide thickness, and additional Raman and PL data (PDF)

## ■ AUTHOR INFORMATION


### Corresponding Author

*E-mail: anna.fontcuberta-morral@epfl.ch.

### ORCID

Anna Fontcuberta i Morral: 0000-0002-5070-2196


### Author Contributions

PL spectroscopy on single NWs was performed by A.G. and L.F. PL spectroscopy on NW ensembles along with the statistical analysis was realized by A.G. Raman spectroscopy on NW ensembles and single NWs along with the analysis was realized by L.F. TEM measurements and analysis were performed by L.F. P.R.G. performed the deposition by sputtering, while A.G. and L.F. performed the deposition by PECVD. Strain analysis and modeling was performed by L.F. NW ordered arrays were obtained by W.K., J.V.-P., M.F., H.P., and L.G., while the ensembles were performed by G.T. A.F.i.M. conceived and designed the experiments and supervised the project. A.G. and L.F. made the figures. A.G., L.F., and A.F.i.M. wrote the manuscript. All authors discussed the results and commented on the manuscript.

### Author Contributions

‡L.F. and A.G. contributed equally.

### Notes

The authors declare no competing financial interest.

## ■ ACKNOWLEDGMENTS

The authors thank funding through SNF by ERAnet-Russia grant no. IZLRZ2-163861, by the NCCR QSIT and project no. 200021-169908, and the H2020 program through the project INDEED.

## ■ REFERENCES


(1) Heiss, M.; et al. *Nat. Mater.* **2013**, *12*, 439−444.

(2) Mancini, L.; Fontana, Y.; Conesa-Boj, S.; Blum, I.; Vurpillot, F.; Francaviglia, L.; Russo-Averchi, E.; Heiss, M.; Arbiol, J.; Morral, A. F. i.; Rigutti, L. *Appl. Phys. Lett.* **2014**, *105*, 243106.

(3) Messing, M. E.; Wong-Leung, J.; Zanolli, Z.; Joyce, H. J.; Tan, H. H.; Gao, Q.; Wallenberg, L. R.; Johansson, J.; Jagadish, C. *Nano Lett.* **2011**, *11*, 3899−3905.

(4) Dick, K. A.; Thelander, C.; Samuelson, L.; Caroff, P. *Nano Lett.* **2010**, *10*, 3494−3499.

(5) Borgström, M. T.; Zwiller, V.; Müller, E.; Imamoglu, A. *Nano Lett.* **2005**, *5*, 1439−1443.

(6) Reimer, M. E.; Bulgarini, G.; Akopian, N.; Hocevar, M.; Bavinck, M. B.; Verheijen, M. A.; Bakkers, E. P. A. M.; Kouwenhoven, L. P.; Zwiller, V. *Nat. Commun.* **2012**, *3*, 737.




DOI: 10.1021/acs.nanolett.7b05402
*Nano Lett.* 2018, 18, 2393−2401

(7) Claudon, J.; Gregersen, N.; Lalanne, P.; Gérard, J.-M. *ChemPhysChem* **2013**, *14*, 2393−2402.
(8) van Dam, D.; Abujetas, D. R.; Paniagua-Domínguez, R.; Sánchez-Gil, J. A.; Bakkers, E. P. A. M.; Haverkort, J. E. M.; Gómez Rivas, J. *Nano Lett.* **2015**, *15*, 4557−4563.
(9) Bulgarini, G.; Reimer, M. E.; Hocevar, M.; Bakkers, E. P. A. M.; Kouwenhoven, L. P.; Zwiller, V. *Nat. Photonics* **2012**, *6*, 455.
(10) Mokkapati, S.; Saxena, D.; Tan, H. H.; Jagadish, C. *Sci. Rep.* **2015**.
(11) Minot, E. D.; Kelkensberg, F.; van Kouwen, M.; van Dam, J. A.; Kouwenhoven, L. P.; Zwiller, V.; Borgström, M. T.; Wunnicke, O.; Verheijen, M. A.; Bakkers, E. P. A. M. *Nano Lett.* **2007**, *7*, 367−371.
(12) Yan, R.; Gargas, D.; Yang, P. *Nat. Photonics* **2009**, *3*, 569.
(13) Hennessy, K.; Högerle, C.; Hu, E.; Badolato, A.; Imamoğlu, A. *Appl. Phys. Lett.* **2006**, *89*, 041118.
(14) Freeman, R.; Willner, I. *Chem. Soc. Rev.* **2012**, *41*, 4067−4085.
(15) Akopian, N.; Wang, L.; Rastelli, A.; Schmidt, O. G.; Zwiller, V. *Nat. Photonics* **2011**, *5*, 230.
(16) Kumar, S.; Trotta, R.; Zallo, E.; Plumhof, J. D.; Atkinson, P.; Rastelli, A.; Schmidt, O. G. *Appl. Phys. Lett.* **2011**, *99*, 161118.
(17) Wang, Y.-B.; Wang, L.-F.; Joyce, H. J.; Gao, Q.; Liao, X.-Z.; Mai, Y.-W.; Tan, H. H.; Zou, J.; Ringer, S. P.; Gao, H.-J.; Jagadish, C. *Adv. Mater.* **2011**, *23*, 1356−1360.
(18) Montinaro, M.; Wüst, G.; Munsch, M.; Fontana, Y.; Russo-Averchi, E.; Heiss, M.; Fontcuberta i Morral, A.; Warburton, R. J.; Poggio, M. *Nano Lett.* **2014**, *14*, 4454−4460.
(19) Signorello, G.; Karg, S.; Björk, M. T.; Gotsmann, B.; Riel, H. *Nano Lett.* **2013**, *13*, 917−924.
(20) Signorello, G.; Lörtscher, E.; Khomyakov, P.; Karg, S.; Dheeraj, D.; Gotsmann, B.; Weman, H.; Riel, H. *Nat. Commun.* **2014**.
(21) Singh, U.; Adenwalla, S. *Nanotechnology* **2015**, *26*, 255707.
(22) Bouwes Bavinck, M.; Zieliński, M.; Witek, B. J.; Zehender, T.; Bakkers, E. P. A. M.; Zwiller, V. *Nano Lett.* **2012**, *12*, 6206−6211.
(23) Stepanov, P.; Elzo-Aizarna, M.; Bleuse, J.; Malik, N. S.; Curé, Y.; Gautier, E.; Favre-Nicolin, V.; Gérard, J.-M.; Claudon, J. *Nano Lett.* **2016**, *16*, 3215−3220.
(24) Matteini, F.; Tütüncüoğlu, G.; Potts, H.; Jabeen, F.; Fontcuberta i Morral, A. *Cryst. Growth Des.* **2015**, *15*, 3105−3109.
(25) Francaviglia, L.; Fontana, Y.; Conesa-Boj, S.; Tütüncüoğlu, G.; Duchêne, L.; Tanasescu, M. B.; Matteini, F.; i Morral, A. F. *Appl. Phys. Lett.* **2015**, *107*, 033106.
(26) Vukajlovic-Plestina, J.; Kim, W.; Dubrovski, V. G.; Tütüncüoğlu, G.; Lagier, M.; Potts, H.; Friedl, M.; Fontcuberta i Morral, A. *Nano Lett.* **2017**, *17*, 4101−4108.
(27) Colombo, C.; Spirkoska, D.; Frimmer, M.; Abstreiter, G.; Fontcuberta i Morral, A. *Phys. Rev. B: Condens. Matter Mater. Phys.* **2008**, *77*, 155326.
(28) Uccelli, E.; Arbiol, J.; Magen, C.; Krogstrup, P.; Russo-Averchi, E.; Heiss, M.; Mugny, G.; Morier-Genoud, F.; Nygård, J.; Morante, J. R.; Fontcuberta i Morral, A. *Nano Lett.* **2011**, *11*, 3827−3832.
(29) Welber, B.; Cardona, M.; Kim, C. K.; Rodriguez, S. *Phys. Rev. B* **1975**, *12*, 5729−5738.
(30) Zardo, I.; Conesa-Boj, S.; Peiro, F.; Morante, J. R.; Arbiol, J.; Uccelli, E.; Abstreiter, G.; Fontcuberta i Morral, A. *Phys. Rev. B: Condens. Matter Mater. Phys.* **2009**, *80*, 245324.
(31) Zardo, I.; Yazji, S.; Marini, C.; Uccelli, E.; Fontcuberta i Morral, A.; Abstreiter, G.; Postorino, P. *ACS Nano* **2012**, *6*, 3284−3291.
(32) Yu, P. Y.; Cardona, M. *Fundamentals of semiconductors: physics and materials properties*; Springer, 2010.
(33) Amaduzzi, F.; Alarcón-Lladó, E.; Russo-Averchi, E.; Matteini, F.; Heiss, M.; Tütüncüoğlu, G.; Conesa-Boj, S.; de la Mata, M.; Arbiol, J.; i Morral, A. F. *J. Appl. Phys.* **2014**, *116*, 184303.
(34) Adachi, S. *J. Appl. Phys.* **1985**, *58*, R1−R29.
(35) Rüffer, D.; Slot, M.; Huber, R.; Schwarze, T.; Heimbach, F.; Tütüncüoğlu, G.; Matteini, F.; Russo-Averchi, E.; Kovács, A.; Dunin-Borkowski, R.; Zamani, R. R.; Morante, J. R.; Arbiol, J.; i Morral, A. F.; Grundler, D. *APL Mater.* **2014**, *2*, 076112.
(36) Hutchinson, W.; Suo, Z. Mixed Mode Cracking in Layered Materials. *Adv. Appl. Mech.* **1991**, *29*, 63−191.
(37) Hua, B.; Motohisa, J.; Ding, Y.; Hara, S.; Fukui, T. *Appl. Phys. Lett.* **2007**, *91*, 131112.
(38) Zhu, J.; Yu, Z.; Burkhard, G. F.; Hsu, C.-M.; Connor, S. T.; Xu, Y.; Wang, Q.; McGehee, M.; Fan, S.; Cui, Y. *Nano Lett.* **2009**, *9*, 279−282.
(39) Schliwa, A.; Winkelnkemper, M.; Bimberg, D. *Phys. Rev. B: Condens. Matter Mater. Phys.* **2007**, *76*, 205324.
(40) Jöns, K. D.; Hafenbrak, R.; Singh, R.; Ding, F.; Plumhof, J. D.; Rastelli, A.; Schmidt, O. G.; Bester, G.; Michler, P. *Phys. Rev. Lett.* **2011**, *107*, 217402.
(41) Kuklewicz, C. E.; Malein, R. N. E.; Petroff, P. M.; Gerardot, B. D. *Nano Lett.* **2012**, *12*, 3761−3765.
(42) Lifshitz, N.; Jayaraman, A.; Logan, R. A.; Maines, R. G. *Phys. Rev. B: Condens. Matter Mater. Phys.* **1979**, *20*, 2398−2400.
(43) Heiss, M.; Conesa-Boj, S.; Ren, J.; Tseng, H. H.; Gali, A.; Rudolph, A.; Uccelli, E.; Peiró, F.; Morante, J. R.; Schuh, D.; Reiger, E.; Kaxiras, E.; Arbiol, J.; Fontcuberta I Morral, A. *Phys. Rev. B: Condens. Matter Mater. Phys.* **2011**, *83*, 1−10.
(44) Wickboldt, P.; Anastassakis, E.; Sauer, R.; Cardona, M. *Phys. Rev. B: Condens. Matter Mater. Phys.* **1987**, *35*, 1362−1368.
(45) Cerdeira, F.; Buchenauer, C. J.; Pollak, F. H.; Cardona, M. *Phys. Rev. B* **1972**, *5*, 580−593.
(46) Adu, K.; Xiong, Q.; Gutierrez, H.; Chen, G.; Eklund, P. *Appl. Phys. A: Mater. Sci. Process.* **2006**, *85*, 287.
(47) Freund, L. B.; Suresh, S. *Thin Film Materials: Stress, Defect Formation and Surface Evolution*; Cambridge University Press, 2004.
(48) Gupta, R.; Xiong, Q.; Mahan, G. D.; Eklund, P. C. *Nano Lett.* **2003**, *3*, 1745−1750.
(49) Krahne, R.; Chilla, G.; Schüller, C.; Carbone, L.; Kudera, S.; Mannarini, G.; Manna, L.; Heitmann, D.; Cingolani, R. *Nano Lett.* **2006**, *6*, 478−482.
(50) Spirkoska, D.; Abstreiter, G.; Fontcuberta I Morral, A. *Nanotechnology* **2008**, *19*, 435704.
(51) Tarraf, A.; Daleiden, J.; Irmer, S.; Prasai, D.; Hillmer, H. *J. Micromech. Microeng.* **2004**, *14*, 317.
(52) Tada, H.; Kumpel, A. E.; Lathrop, R. E.; Slanina, J. B.; Nieva, P.; Zavracky, P.; Miaoulis, I. N.; Wong, P. Y. *J. Appl. Phys.* **2000**, *87*, 4189−4193.
(53) Jansen, F.; Machonkin, M. A.; Palmieri, N.; Kuhman, D. *J. Appl. Phys.* **1987**, *62*, 4732−4736.
(54) Straumanis, M. E.; Krumme, J. P.; Rubenstein, M. *J. Electrochem. Soc.* **1967**, *114*, 640−641.
(55) Ettenberg, M.; Paff, R. J. *J. Appl. Phys.* **1970**, *41*, 3926−3927.



DOI: 10.1021/acs.nanolett.7b05402
*Nano Lett.* 2018, 18, 2393−2401